第 34 卷第 1 期
2015 年 2 月

红 外 与 毫 米 波 学 报
J. Infrared Millim. Waves

Vol. 34, No. 1
February, 2015

文章编号:1001 - 9014(2015)01 - 0010 - 04

DOI:10. 3724/SP. J. 1010. 2015. 00010

Thermal crosstalk characteristics in high-power 808 nm AlGaAs/GaAs laser diode bars

QIAO Yan-Bin, CHEN Yan-Ning*, ZHAO Dong-Yan, ZHANG Hai-Feng

(Beijing Nari Smart-Chip Microelectronics Technology Company, Ltd., Beijing 100192, China)

Abstract: The thermal crosstalk characteristics in high-power 808 nm AlGaAs/GaAs laser diode bar were investigated experimentally and theoretically using infrared thermography and finite element method. We have performed the steady-state and transient analysis. A detailed profile of thermal crosstalk in laser diode bar was presented in this paper. The steady-state temperature rise has a logarithmical dependence on the total operation current, and the thermal crosstalk between emitters increases with the current density. Furthermore, the transient thermal analysis suggested that the thermal crosstalk occurred mainly in chip. Using thermal resistance parallel connection model, we explained the phenomena that the time constant of chip decreased with the increase of total operation current.

Key words: semiconductor technology, thermal crosstalk characteristics, infrared thermography, finite element method, high-power 808 nm AlGaAs/GaAs laser diode bar

PACS: 71.55.Eq, 72.15.Eb, 85.60.Bt

高功率 808 nm AlGaAs/GaAs 基半导体激光器巴条的热耦合特征

乔彦彬, 陈燕宁*, 赵东艳, 张海峰

(北京南瑞智芯微电子科技有限公司,北京 100192)

摘要:利用红外热成像技术和有限元方法在实验和理论上研究了高功率 808 nm 半导体激光器巴条热耦合特征,给出了稳态和瞬态热分析,呈现了详细的激光器巴条热耦合轮廓.发现器件稳态温升随工作电流呈对数增加,热耦合也随之增加且主要发生在芯片级.另外,作者利用热阻并联模型解释了芯片级热时间常数随工作电流减小的现象.

关　键　词:半导体技术;热耦合特征;红外热成像技术;有限元;高功率 808 nm AlGaAs/GaAs 基半导体激光器巴条

中图分类号:71.55.Eq, 72.15.Eb, 85.60.Bt　　**文献标识码**:A

Introduction

In recent years, as the output power of laser diode bars (LDBs) with AlGaAs active regions continues to increase, LDBs have a wide range of applications including solid-state laser pumping, materials processing, optical communications, and printing machines[1-2]. However, the reliability of such high-power devices remains a critical factor that limits further applications. Several efforts have been attempted to analyze the degradation of LDBs[3-6] and to improve the performance[7-8]. Thermal properties in LDBs are main issue for improving the optical characteristics and lifetime of these bars. For example, changes of band gap with the device temperature can result in a tuning of the emission wavelength[9]. Aging tests have demonstrated that the lifetime of LDBs decreased exponentially with the temperature of active region, which suggested that the degradation of the LDBs strongly depended on their thermal performance[10]. The optimized fill factors related to optical power in laser diode bar were obtained with respect to thermal resistance[11]. Especially, as the output power of the emitters increases, the thermal crosstalk between emitters be-

---

Received date: 2013 - 12 - 26, **revised date**: 2014 - 04 - 25　　**收稿日期**:2013 - 12 - 26, **修回日期**:2014 - 04 - 25

Foundation items: Supported by National Natural Science Foundation of China (61376077); the Beijing Natural Science Foundation of China (4132022)

Biography: QIAO Yan-Bin (1980-), male, Beijing, Ph. D. Research area is the reliability of semiconductor devices and IC chip. E-mail: ybqiao@126.com

* **Corresponding author**: E-mail: chenyanning@sgepri.sgcc.com.cn

comes more significant, which affects strongly the performance of the LDBs[12].

We have analysis the transient thermal properties of LDBs using diode forward voltage method in previous works[13,14], However, up to now, the thermal crosstalk characteristics in high-power LDBs is not entirely clear. In particular, how the thermal crosstalk affects the performance of the LDBs when the optical power increases. In this paper, we analyzed experimentally and theoretically the thermal crosstalk characteristics in high-power AlGaAs/GaAs LDBs in detail using infrared thermography and finite element method(FEM).

1 Sample details

A high-power laser diode bar is an array of parallel single emitter, which shares a common substrate and heat sink. The commercial 808 nm emitting high-power LDBs grown on(100) n-type substrate by metal-organic chemical vapor deposition were used in this work, and they were designed for 10-W continuous-wave operation with AlGaAs/GaAs quantum well structure. Figure 1(a) presents the schematic diagram of the LDB. The bar contained a linear array of nine emitters. Each emitter has dimensions of 1 000 × 100 × 103 μm^3 (length × width × heigh), and separated by 200 μm isolation regions. Each emitter had an individual p-side electrode while all emitters shared a common n-side electrode so that each emitter could operate individually during measurements. The threshold current density and slope efficiency of each emitter are about 0.21 kA/cm^2 and 0.96 W/A, respectively. The bar was mounted p-side up onto a copper heat sink with indium solder.

2 Experimental details and theory model

The temperature data of emitters including output facet were obtained from a FLIR System SC5700 camera working in the 2.5 ~ 5.1 μm range images with a temperature resolution of 20 mK. The thermal infrared camera recorded the images with a frequency of 115 Hz(1 ms integration time, 7.6 ms dead time) and a spatial resolution of about 3.0 μm per pixel. The laser diode radiation coming from interband quantum well transitions was rejected using a Ge-wafer as a filter in order to avoid additional heating of the lens and the detector during laser operation. The Ge-wafer with 1 mm thickness can absorb the 808 nm laser because the band gap of Ge-wafer(~0.744 eV) is less than that of active region of the LDBs. Quantitative thermal measurements of electronic systems require a thorough calibration procedure. The calibration characteristics have been carried out in the range from 25 ℃ to 80 ℃ in 5 ℃ step, the temperature of non-operating laser diodes was controlled by water-cooling temperature controller. For each temperature setting a thermal image containing the output facet of the device was captured with the camera. Thus, the temperature differences related to this calibrated reference were obtained. The device under test was attached on a fixed-temperature(25 ℃) plate with water-cooling temperature controller. The diagram of the experimental setup for measuring the temperature of emitters in laser diode bars is shown in Fig. 1b.

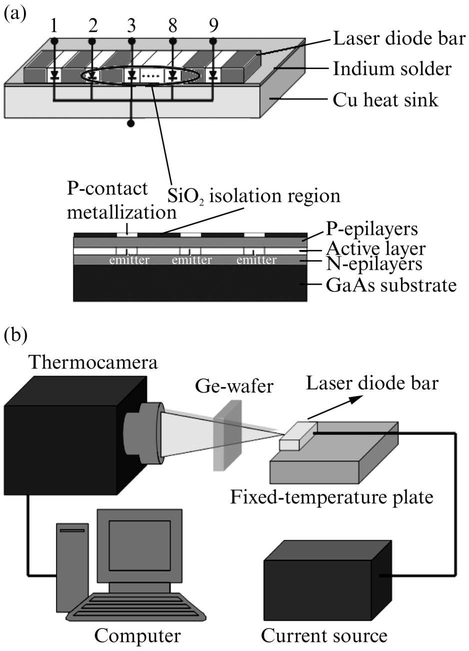

Fig. 1 (a) The schematic diagram of the 808 nm AlGaAs/GaAs laser diode bar and the structure of the chip. (b) Diagram of the experimental setup for measuring the temperature of emitters in laser diode bars

图 1 (a)808 nm AlGaAs/GaAs 基半导体激光器巴条及其芯片结构示意图,(b)激光器巴条发光单元温度测试步骤示意图

Based on the three dimensions(3D) FEM, the temperature distribution in the device was calculated using the steady-state heat transfer equation:

$$0 = \nabla(k\ \nabla T) + q \quad , \qquad (1)$$

where k and q are the thermal conductivity of the material and generated-heat density from the heat source, respectively.

The boundary conditions consist of two different types: one is Neumann boundary which is assumed at all the laser air interfaces to specify the inward heat flux, another is the Dirichlet boundary which is used at the indium-solder/copper heat sink interface. The Dirichlet boundary assumes that the Cu-heat sink is of infinite thermal conductivity. The material parameters used in the calculations were obtained from Ref. 15. In the calculation model, the lasing emitter is defined as the heat source, and the loaded heat power density is equal to the forty percent of the electrical power density based on 60% conversion efficiency of electrical input into optical output.

3 Results and discussion

Thermal crosstalk between emitters reflects how the operated emitters affect each other with respect to thermal properties. In other words, there should be no thermal crosstalk when a single emitter is operated. Figure 2(a) presents the infrared images of emitter 5 at current density of 0.5 and 1.0 kA/cm^2, and as depicted in Fig. 2(b), the temperature rise of output facet in emitter 5 as a function of the operating current is measured using the infrared thermography while other emitters are un-operated. The temperature rises of active region have a linear relationship with the operating current which reflects the thermal profile without thermal crosstalk. Subsequently, we add the number of operated emitters as the sequence: 5→4→6→3→7→2→8→1→9. Each added emitter is loaded with a current of 0.5 A. The emitter 5 is applied first a current of 0.5 A, and the total current applied to the LDB increases with a step of 0.5 A, that is, $I_{total} = n \times 0.5$ A($n = 1, 2, 3 \cdots 9$). Then, we measured the steady-state temperature rise of emitter 5 at each current increment as shown in Fig. 3. It is found that the steady-state temperature rise of emitter 5 increases logarithmically with the total operation current which is consistent with that obtained by diode forward voltage method[13]. The measured results show that when all emitters are operated the temperature rise of central emitter 27.4 ℃ is higher than that of edge emitters about 5 ℃, which is attributed to that the edge emitters have advantageous heat conduction conditions compared to the central emitter. The steady-state temperature rise of emitter 5 can be expressed by the equation below:

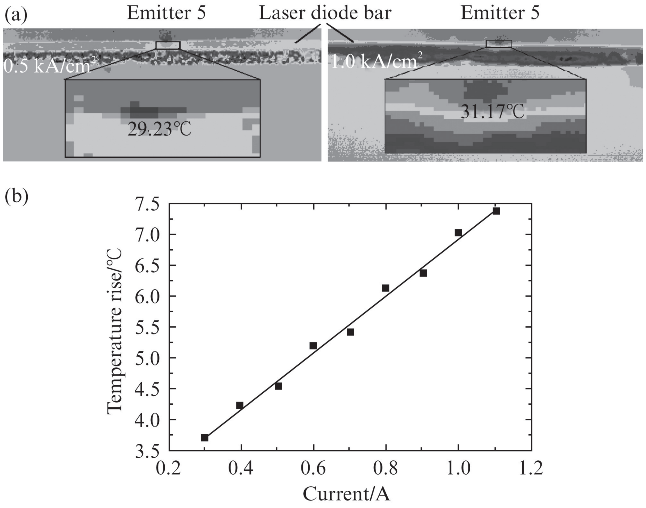

Fig. 2 (a) The infrared images of emitter 5 at current density 0.5 and 1.0 kA/cm². (b) The temperature rise of output facet in emitter 5 as a function of the operation current measured using the infrared thermography when emitter 5 operates individually

图 2 (a)在电流密度 0.5 和 1.0 kA/cm² 下,发光单元 5 的红外热图像,(b)发光单元 5 的腔面温度随其工作电流的变化关系

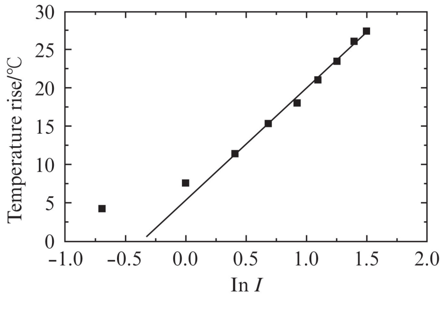

Fig. 3 The measured steady-state temperature rise of emitter 5 at each current increment(0.5 A) using the infrared thermography. The solid line presents the numerical fitting result

图 3 发光单元 5 的稳态温升随总工作电流的变化关系,总工作电流每次增加 0.5 A

$$\Delta T = \Delta T_0 + A \ln I \quad , \quad (2)$$

where ΔT is the steady-state temperature rise, and ΔT_0 is the initial temperature rise of emitter 5 for initial current (0.5 A). The coefficient A is a constant and proportional to the temperature increase rate. The magnitude of coefficient A reflects the degree of thermal crosstalk between emitters under different total current. Such results are different from that when only emitter 5 is operated, which originates from the thermal crosstalk between emitters. Consequently, in order to prove the experimental results, we simulate the steady-state temperature rise according to the measuring process used in experiment above under different current density, based on the FEM. The structure of sample used in simulations is the same as that used in experiments. The steady-state temperature rise of emitter 5 is plotted in Fig. 4a as a function of the logarithm of the total current at different current density, which also shows a linear relationship with the logarithm of total current as that obtained from infrared thermography. In addition, we extract the coefficient A presented in Fig. 4b. The values of the coefficient A increase with the current density, and displaying a linear relationship with the current density which indicate that the thermal crosstalk between emitters increases with the current density.

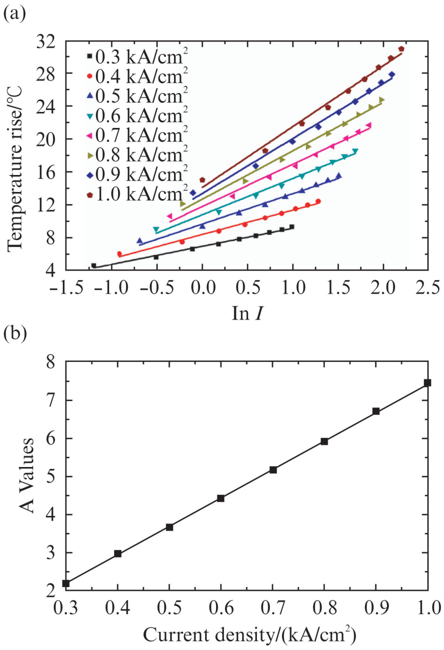

Fig. 4 (a) The calculated steady-state temperature rise of emitter 5 varies with the operating current under different current density. (b) The coefficient A values as a function of current density

图 4 (a)模拟计算得到发光单元 5 的稳态温升随电流密度的变化,(b)系数 A 随电流密度变化关系

We further investigated the thermal crosstalk based on transient thermal properties of LDBs using infrared thermography. Figure 5a displays the time resolution of temperature rise of emitter 5 at different total operating current. During the measurement, the sequence of the operating current is set as that used in measuring the steady-state temperature rise above. Based on the Refs. 13 and 16, the transient temperature rise can be well approximated by the following analytic expression:

$$\Delta T = \sum_{i=1}^{2} T_i\left[1-\exp\left(-\frac{t}{\tau_i}\right)\right]\text{and } \tau_i = R_i \times C_i \quad ,(3)$$

where T_i is the temperature rise of the i^{th} component in the thermal conduction path (from chip to heat sink), each with a time constant τ_i. R_i and C_i is the thermal resistance and thermal capacitance. Changes in the time constant τ_i with operation current reflect the thermal crosstalk characteristics between emitters. Based on the Eq. (3), the whole data in Fig. 5a are well reproduced by numerical fitting using the least square method in Origin 8.0 software. The time constant τ_i is plotted in Fig. 5b with a ±10% deviation. The temperature rise of the chip is dominated by the time constant τ_1 which changes from 123.3 ms to 72.6 ms with increasing operation current. With regard to the magnitude of the values this result is consistent with that obtained by infrared thermography in Ref. 16 but is higher than that measured using the diode forward voltage method in Ref. 13 This may be attributed to the difference of the measuring method. Using diode forward voltage method the average temperature of the chip was measured, while the temperature of certain local spot was measured by infrared thermography.

The variation of time constant τ_1 can be extracted from the thermal equivalent circuit, which is shown in Fig. 5c. In the p-side up structure, the heat generated from active region will flow to indium solder, then to heat sink. The total thermal resistance of chip changes with the number of operated emitters, which is expressed as follows:

$$R_1 = \frac{1}{N}R_{em} \quad , (4)$$

where R_1 and R_{em} represents the total thermal resistance of operated emitters and each emitter, respectively, and N is the number of operated emitters. Based on Eq. (4), the total thermal resistance R_1 decreases as the increase of the number of operated emitters, and the time constant τ_1 decreases accordingly under the thermal capacitance C_1 remaining constant. The changing trend of the time constant τ_1 of emitter 5 indicates that the thermal crosstalk between emitters increases as total operating current increases. Meanwhile, the time constant τ_2 which is determined by the properties of the solder/heat sink interface and package does not change almost as the operation current increases. The changing trend of the time constant τ_1 and τ_2 agrees well with that obtained form the diode forward voltage method in Ref. 13. These results suggest that the thermal crosstalk mainly occurs within the chip, rather than the solder/heat sink interface and package, and the thermal crosstalk between emitters increases with the total operating current. The results suggest that under constant total working currents, low current density and small emitter width are favorable to decreasing the chip temperature in order to improve the LDBs reliability. We can conclude that the infrared thermography is a useful method for investigating the thermal crosstalk characteristics in LDBs.

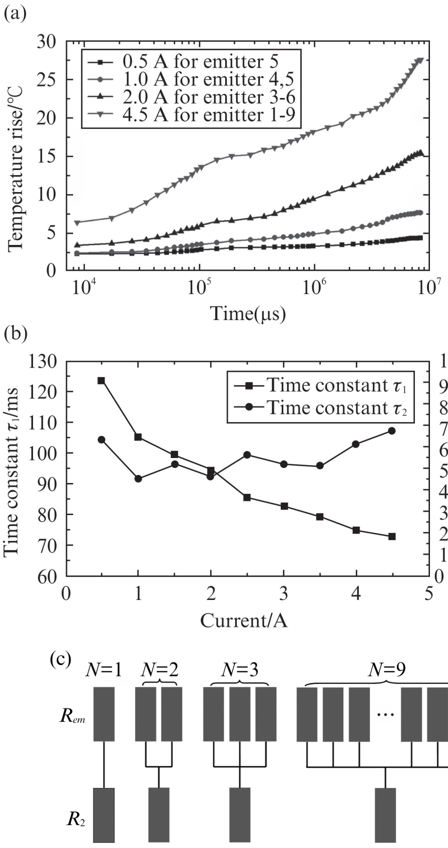

Fig. 5 (a) The transient temperature rise of emitter 5 at different operating current. (b) The changes of time constant τ_1 and τ_2 with the operating current. (c) The model for explaining the phenomena that time constant τ_1 decrease with the operating current
图 5　(a)发光单元 5 在不同总工作电流下的瞬态温升曲线，(b)时间常数 τ_1 和 τ_2 随总工作电流的变化，(c)解释时间常数 τ_1 随工作电流变化关系的模型图

4 Conclusions

We performed steady-state and transient analysis to identify the thermal crosstalk characteristics in high-power AlGaAs/GaAs LDBs using infrared thermography and finite element method. The devices used in experiments were designed specifically in which each emitter can be operated individually. The steady-state temperature rise of the central emitter among operated emitters has a linear relationship with the logarithm of total operating current and thermal crosstalk increases with the current density. The thermal crosstalk profile was given based on the time constant from the transient measurements which suggested that the thermal crosstalk mainly occurred within the chip rather than solder/heat sink interface and package. The thermal crosstalk between emitters increases with the current density, thus, under constant total working currents, low current density and small emitter width are desirable for devices design. We explain the phenomena that the time constant of chip decreases with total operating current. The fundamental understanding of the thermal crosstalk characteristics between emitters of AlGaAs/GaAs LDBs is helpful for further improving the performance of LDBs.

（下转第 35 页）

[2] WEI Hua. The prospects for THz detection techniques development [J]. *Infrared Technology*(魏华. 太赫兹探测技术发展与展望. **红外技术**), 2010, **32**(4): 231 – 234.

[3] CAO Jun-Cheng. Semiconductor terahertz sources, detectors and applications[M]. Beijing: Science Press(曹俊诚. 半导体太赫兹源、探测器与应用. 北京: 科学出版社), 2012: 5 – 7.

[4] YANG Guang-Kun, YUAN Bin, XIE Dong-Yan, *et al*. Analysis on the use of THz technology in the military application [J]. *Laser & Infrared*(杨光鲲,袁斌,谢东彦等. 太赫兹技术在军事领域的应用. **激光与红外**), 2011, **41**(4): 376 – 380.

[5] SHEN Wen-Zhong. Novel Homojunction Far-infrared Detectors [J]. *J. InfraredMillim. Waves*(沈文忠. 新型同质结构远红外探测器. **红外与毫米波学报**), 2000, **19**(3): 161 –168.

[6] Perera A G U, Yuan H X, Gamage S K, *et al*. GaAs multilayer p^+ – i homojunction far-inrared detectors [J]. *J. Appl. Phys*, 1997, **81**(7): 3316 – 3319.

[7] SHEN Wen-Zhong, Perera A G U Francombe, M H, *et al*. Effect of emitter layer concentration on the performance of GaAs p-i homojunction far-infrared detectors: a comparison of theory and experiment [J]. *IEEE Trans. Electron Devices*, 1998, **45**(8): 1671 – 1677.

[8] ZHENG Mei-Mei, ZHANG Yue-Heng, SHEN Wen-Zhong. Performance optimization of resonant cavity enhanced n-GaAshomojunction far-infrared detectors: A theoretical study [J]. *J. Appl. phys*, 2009, **105**(8): 4515 – 4520.

[9] DENG Guo-Gui, ZHANG Yue-Heng, SHEN Wen-Zhong. Design of a top mirror for the n-GaAshomojunction far-infrared/terahertz detectors [J]. *J. Appl. phys*, 2010, **108**(7): 4509 – 4513.

[10] A G U Perera, H X Yuan, M H Francombe. Homojunction internal photoemission far-infrared detectors: Photoresponse performance analysis [J]. *J. Appl. phys*, 1995, **77**(2): 915 – 924.

[11] SHEN Wen-Zhong, A G U. Perera, LIU Hui-Chun, *et al*. Bias effects in high performance GaAshomojunction far-infrared detectors [J]. *Appl. phys. lett*, 1997, **71**(18): 2677 – 2679.

[12] Yuan H X, Perera A G U, Dark current analysis of Si homojunction interfacial work function internal photoemission far-infrared detectors [J]. *Appl. phys. lett*, 1995, **66**(17): 2262 – 2264.

[13] Harald Schneider, LIU Hui-Chun. Quantum well Infrared photodetectors: Physics and Applications[M]. New York: Springer Publishing Company, 2007, 71 – 72.

[14] Blakemore J S. Semiconducting and other major properties of gallium arsenide [J]. *J. Appl. phys*, 1982, **53**(R123).

* * *

(上接 13 页)

References

[1] John G. E, Mitral V, Gerald S. B, *et al*. High Power Diode Laser Arrays [J]. *IEEE Journal of Quantum Electronics*, 1992, **28**(4): 952 – 965.

[2] Treusch H G, Ovtchinnikov A, He X, *et al*. High-brightness semiconductor laser sources for materials processing: stacking, beam shaping, and bars [J]. *IEEE Journal of Selected Topics in Quantum Electronics*, 2000, **6**(4): 601 – 614.

[3] Ziegler M, Tomm J W, Elsaesser T, *et al*. Real-time thermal imaging of catastrophic optical damage in red-emitting high-power diode lasers [J]. *Applied Physics Letters*, 2008, **92**(10): 103514.

[4] Qiao Y B, Feng S W, Xiong C, *et al*. Spatial hole burning degradation of AlGaAs/GaAs laser diodes. *Applied Physics Letters*, 2011, **99**(10): 103506.

[5] Bull S, Tomm J W, Larkins E C. Identification of degradation mechanisms in high-power laser bars using by-emitter degradation studies [J]. *Journal of Materials Science: Materials in Electronics*, 2008, **19**(1): s145 – s149.

[6] Tomm J W, Ziegler M, Oudart M, *et al*. Gradual degradation of GaAs-based quantum well lasers, creation of defects, and generation of compressive strain [J]. *physica status solidi* (*a*), 2009, **206**(8): 1912 – 1915.

[7] Rinner F, Rogg J, Kelemen M T, *et al*. Facet temperature reduction by a current blocking layer at the front facets of high-power InGaAs/AlGaAs lasers [J]. *Journal of applied physics*, 2003, **93**(3): 1848 – 1850.

[8] Hempel M, Tomm J W, Hennig P, *et al*. Emission properties of diode laser bars during pulsed high-power operation [J]. *Semiconductor Science and Technology*, 2011, **26**(9): 092001.

[9] Liu X, Hu M H, Caneau C G, *et al*. Thermal management strategies for high power semiconductor pump lasers [J]. *IEEE Transactions on Components and Packaging Technologies*, 2006, **29**(2): 268 – 276.

[10] Fukuda M. Reliability and degradation of semiconductor lasers and LEDs[M]. *Boston: Artech House*, 1991.

[11] Laikhtman B, Gourevitch A, Westerfeld D, *et al*. Thermal resistance and optimal fill factor of a high power diode laser bar [J]. *Semiconductor science and technology*, 2005, **20**(10): 1087 – 1095.

[12] Amuzuvi C K, Bull S, Tomm J W, *et al*. The impact of temperature and strain-induced band gap variations on current competition and emitter power in laser bars [J]. *Applied Physics Letters*, 2011, **98**(24): 241108.

[13] Qiao Y, Feng S, Xiong C, *et al*. The thermal properties of AlGaAs/GaAs laser diode bars analyzed by the transient thermal technique [J]. *Solid-State Electronics*, 2013, **79**: 192 – 195.

[14] Li J, Feng S, Zhang G, *et al*. Thermal analysis of high power laser diodes with multiple emitters [J]. *Infrared and Laser Engineering*(李静婉,冯士维,张光沉,等. 多发光区大功率激光器的热特性分析. **红外与激光工程**), 2012, 41(8):2027 – 2032.

[15] Martín-Martín A, Avella M, Iñiguez M P, *et al*. Thermomechanical model for the plastic deformation in high power laser diodes during operation [J]. *Journal of Applied Physics*, 2009, **106**(7): 073105.

[16] Ziegler M, Weik F, Tomm J W, *et al*. Transient thermal properties of high-power diode laser bars [J]. *Applied physics letters*, 2006, **89**(26): 263506.